

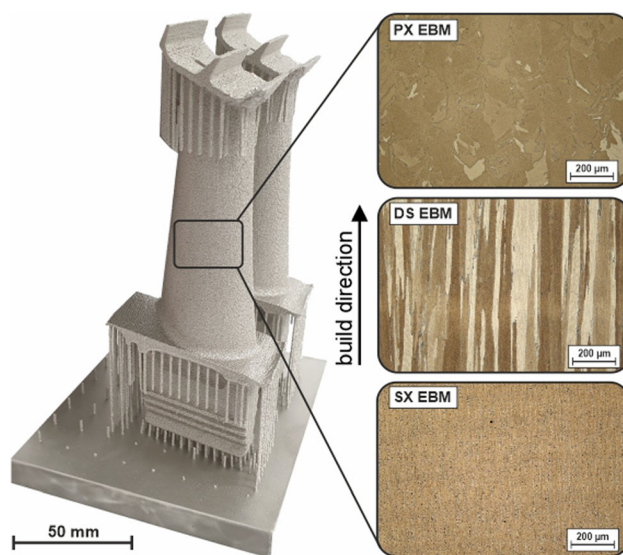


Electron Beam Based Additive Manufacturing of Alloy 247 for Turbine Engine Application: From Research towards Industrialization

MARKUS RAMSPERGER and SIMON EICHLER

In this contribution it will be shown how the metal powder bed fusion technology electron beam melting (EBM) enables a successful crack- and defect-free processing of the non-weldable Ni-based superalloy Alloy 247. Besides a defect-free processing, EBM process capabilities offer unique opportunities to tailor the microstructure according to material requirements for high-temperature applications. It could be demonstrated that EBM material properties are comparable or even better than traditionally casted Alloy 247 material. Tailored polycrystalline and columnar microstructures were achieved by process parameter adoption for solidification control. The EBM as-built microstructure was characterized by conventional metallography techniques and the results were used to define an adopted HIP + heat-treatment cycle which was applied prior to mechanical testing. Thus, corresponding mechanical and microstructural properties in different conditions will be presented and discussed to show EBM material capabilities. As a result, directionally solidified (DS) EBM material can achieve similar creep performance as DS cast material, despite an observed fine-grained “micro-DS” structure in EBM.

Graphical Abstract



<https://doi.org/10.1007/s11661-022-06955-0>
© The Author(s) 2023

MARKUS RAMSPERGER is with the GE Additive Arcam EBM Center of Excellence, Designvägen 2, 43533 Mölnlycke, Sweden. Contact e-mail: markus.ramsperger@ge.com SIMON EICHLER is with the GE Additive, Rudolf-Diesel-Straße 14, 96215 Lichtenfels, Germany

Manuscript submitted July 31, 2022; accepted December 28, 2022.

Article published online March 1, 2023

I. INTRODUCTION

NI-BASED superalloys have a long history within the high-pressure turbine (HPT) and low-pressure turbine (LPT) section of turbine engines, thanks to their superior high-temperature properties above 800 °C.

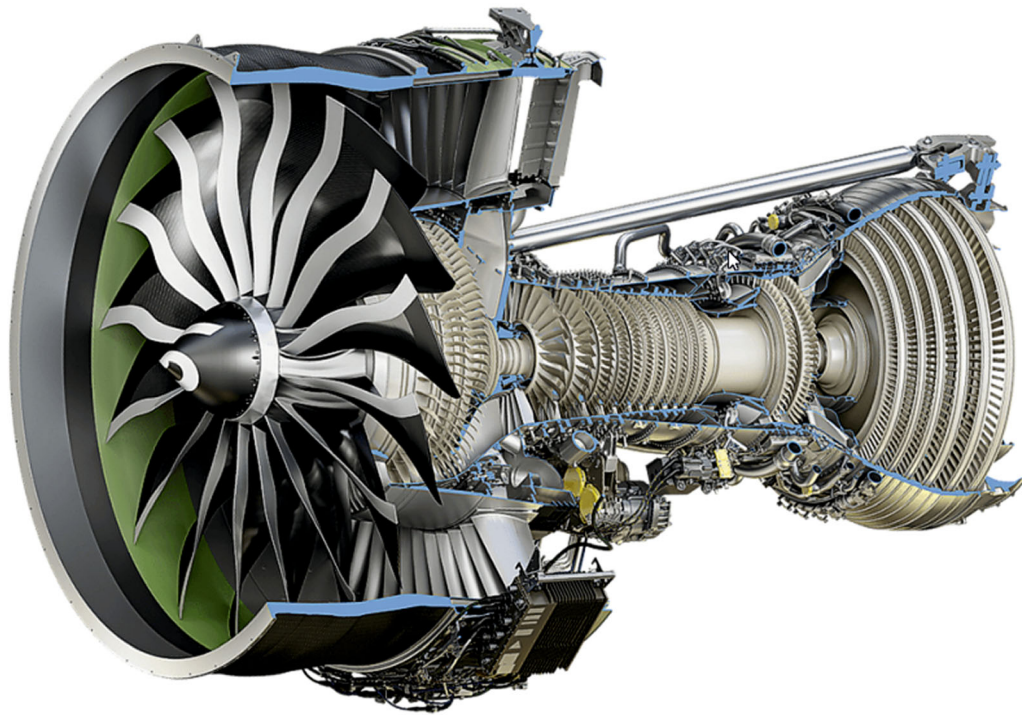


Fig. 1—Schematic of an GE9X aero engine. Besides new and innovative high-temperature materials like stage 5 and 6 TiAl blades in the LPT, many components within the HPT and LPT are made off Ni-based Superalloys in different microstructure configurations [courtesy of GE Aviation].

Large R&D efforts over the last 50 years resulted in an expansion of their high-temperature capabilities by developing new alloys and advanced casting technologies. Nevertheless, high demands on material qualification and validation efforts resulted in long development times to bring new alloys into service. Therefore, well-established, and well-known Ni-based alloys (from the 70's) were still used in the latest versions of the turbine engines. A recent example is the GE9X engine depicted in Figure 1. Besides new materials like Titanium Aluminides (TiAl), almost half of all used components are made from Ni-based Superalloys in different microstructural configurations.

One example is the flow-path hardware of the Turbine Center Frame, where Alloy 247 (MAR M247) is used for several components. This conventionally cast (as CC, equiaxed) Superalloy was developed in the early 1970's by the Martin Metals Corporation and show excellent creep and oxidation properties due to the high γ' volume fraction of > 60 pct and a high content of refractory elements. Alloy 247 has a good castability due to the addition of Hf and is still one of the most common CC materials for static and rotating components as vanes, shrouds, nozzles and turbine blades. Alloy 247 can also be cast as directionally solidified (DS) or single crystal (SX) material,^[1] however, the alloy was originally not optimized for anisotropic configurations. The need for even better creep and fatigue performance for new engine generations led to modifications of MAR M247 by Cannon Muskegon in the late 1970's. By lowering the C, Zr, Ti, Si and S content, grain

boundary cracking could be handled during DS casting and carbide microstructure improvement was achieved. The result was the MAR-M247 DS derivate CM247LC.^[2]

Several Ni-based Superalloys like IN718, IN625 or HastalloyX became well-established within the AM materials portfolio of various machine manufactures. Since metal powder bed fusion Additive Manufacturing (AM) evolved over the past 15 years. These alloys are already successfully integrated into today's state of the art AM serial production of aerospace components.

Electron beam melting (EBM) and laser powder bed fusion (L-PBF) are the two most established powder bed fusion technologies to date. As both EBM and LPBF utilize an energized beam for material consolidation, they are closely linked to welding physics and suffer from a high crack-susceptibility during processing of Superalloys with a high-gamma prime content like Alloy 247. The alloy was originally designed for casting application where predominant slow solidification velocities and low gradients are present, not for rapid solidification and high gradients occurring in L-PBF and EBM processing. These solidification conditions lead to high level of residual stresses within the components and the layer-based manufacturing to a consistent partial remelting of already solidified material. This can cause several types of cracking in different processing steps and during solidification.^[3-8] Crack-sensitivity issues of Alloy 247 in welding is well-known and the alloy is therefore referred to as a "non-weldable" or "poorly weldable" material.

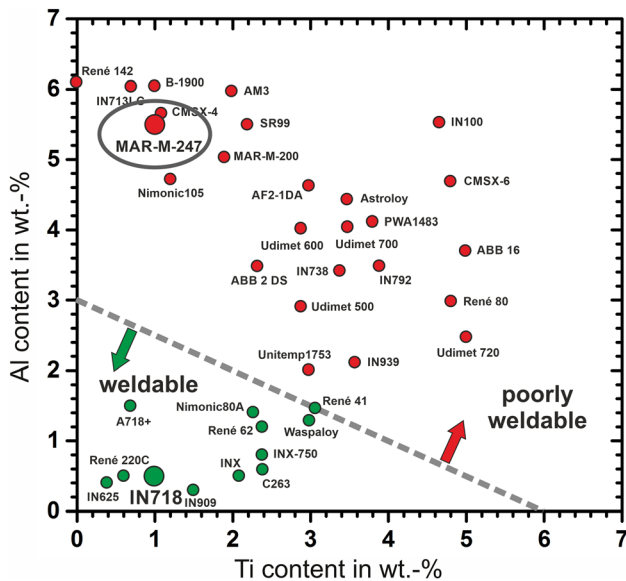


Fig. 2—Weldability chart of several Ni-based Superalloys in terms of their Al and Ti content, adapted and reprinted with permission from Ref. [11]. Alloy 247 as a non-weldable alloy is highlighted in the regime for poorly weldable alloys.

An overview about the weldability of Ni-based Superalloys in comparison to their aluminum (Al) and titanium (Ti) content is given by the chart in Figure 2. Al and Ti as gamma prime forming elements are controlling the amount of γ' in the alloy and act as an indicator for their weldability.^[9] Typically, alloys show good weldability below the dotted line depicted at 3 wt pct Al and 6 wt pct Ti. Nevertheless, besides the amount of γ' in an alloy, weldability is also depending on the base material, grain microstructure and grain size distribution.^[10]

As shown in Figure 2, Alloy 247 is found deep in the non-weldable field of the weldability chart. Several attempts to process commercially available powder chemistries of Alloy 247/CM247LC using Selective Laser Melting were reported in literature and severe crack formation in the consolidated material was observed even if the energy input was adapted and new scan strategies/patterns were applied.^[12–14]

Crack healing by a subsequent HIP treatment as a mitigation approach proved to be non-trivial in terms of process handling. For successful crack-mitigation in components a crack-free and dense shell is required. Furthermore, rapid solidification in L-PBF can suppress the main γ' precipitation during processing and a heat-treatment can trigger strain-age cracking by γ' re-precipitation in the material during the heating phase.^[15]

Approaches to adapt the chemistry for L-PBF towards a better processability by reducing and controlling the content of minor elements like Si can reduce the overall remaining crack-density in the material. Nevertheless, an improved AM processability by reducing minor element contents can have a negative impact and impair mechanical high-temperature properties of the material.^[3,16,17]

In general, the same cracking mechanisms apply to EBM and L-PBF manufacturing of high-gamma prime Superalloys. However, the EBM process has proven to be less sensitive to crack formation due to the inherent high process temperatures and the high degree of flexibility in beam deflection and focusing. Successful EBM processing of several crack-prone alloys such as Inconel 738, Rene142 and CMSX-4 were reported in literature where low remaining crack-density or defect-free specimens were achieved.^[18–20] Basically, a lower remaining level of residual stresses in the material during EBM processing is achieved utilizing preheating and heating sequences within each layer by governing the heat flux. Furthermore, the flexibility in the e-beam movement allows advanced melting strategies and enables control on melt pool shape, solidification behavior and corresponding temperature gradients within the melt pool. As a result, cracking issues can be mitigated and the remaining microstructure can be controlled in that way, to produce “micro casting” CC, DS and even SX grain microstructures.^[19,21,22]

In terms of EBM processing of MAR M247 only a few investigations can be found in literature.^[23] It seems that the crack-susceptibility of the alloy is enhanced and processing more difficult in comparison to other chemistries. A reason for this could be liquid film formations at the grain boundaries due to segregation effects of alloying elements (minor elements).^[24]

EBM processing conditions lead to a fully developed microstructure enclosing γ' and carbide precipitation already in the as-built condition. This can be attributed to the high build temperatures > 1000 °C and isotherm process conditions which represents an *in-situ* heat-treatment of the consolidated material during EBM processing. High solidification velocities in EBM lead to very fine and homogenous as-built microstructures up to an order of magnitude smaller than in those achieved in investment casting. EBM material is almost homogenized in the as-built condition. This results in high-temperature mechanical properties in as-built EBM condition at least similar as-cast and heat-treated material. In addition, LCF and HCF material properties can benefit from smaller EBM pore (defect) sizes in comparison to cast material. If a subsequent HIP heat-treatment is applied, potentially remaining defects can be mitigated, or their size and amount can be further decreased leading to superior EBM material properties.^[20,25–29]

In this contribution the possibility for fabrication of Alloy 247 components by EBM is demonstrated. Resulting microstructures and mechanical properties for as-built and heat-treated conditions are discussed.

II. MATERIALS AND METHODS

A. Material

The powder used for this work was a gas atomized Alloy 247 powder provided by *Praxair Surface Technologies* (Ni-335-7). The particle size distribution was measured using a Malvern Mastersizer 3000 laser diffraction system to $D_{10} = 46$ μm ; $D_{50} = 68$ μm and

$D_{90} = 100 \mu\text{m}$. The chemical analysis is shown in Table I. It is worth to mention, that the Hf content is on the lower end and C content on the upper end of the specification.

The powder morphology was evaluated using a metallographic cross-section depicted in Figure 3. Powder particles were mainly spherical with minor number of irregular-shaped particles and satellites. Noticeable remaining gas porosity within the powder particles are typical in gas atomization powder manufacturing route.

B. EBM Processing of Alloy 247

The powder was processed in a modified GE Additive ArcamEBM Q10plus machine. The standard Q10plus Electron Beam Unit (EBU) was replaced by a new generation EBU which is standard for state of the art ArcamEBM SpectraH systems. The system operated under controlled 2×10^{-3} mbar He atmosphere, 60 kV acceleration voltage and layer thicknesses of 50 and 70 μm . The specimen temperature was constantly kept $> 1000 \text{ }^\circ\text{C}$ during the build process using a defocused e-beam for build surface Preheating and Heating during the melt process. The left panel of Figure 4 shows a snapshot of the EBM process after material consolidation and visualizes the elevated process temperatures. Mechanical test specimens on a start plate after powder removal are illustrated in Figure 4 (right).

For mechanical properties evaluation and microstructure evolution investigations, round shaped specimens with a diameter of $\varnothing = 15 \text{ mm}$ and sample height $h = 75 \text{ mm}$ were built on a stainless-steel start plate utilizing pin support structures.

All specimens were produced by varying normalized beam velocity v between 500 and 800 mm/s, focus offset FO between 15 and 35 mA and the volume energy VE between 80 and 135 J/mm^3 . Volume energy is defined as:

$$\text{Volume energy} = \frac{\text{acceleration voltage} \cdot \text{beam current}}{\text{beam velocity} \cdot \text{offset} \cdot \text{layer thickness}}$$

$$\left[\frac{\text{J}}{\text{mm}^3} \right]$$

For investigation of the microstructure evolution the parameter sets shown in Table II were applied. Specimens for tensile testing in PX configuration were produced using Parameter 1 and for DS configuration Parameter 7.

C. Heat- and HIP Heat-Treatment

A solution heat-treatment study was performed to identify the suitable heat-treatment temperature range for EBM processed Alloy 247. Polycrystalline (PX) material was chosen for this experiment. Corresponding holding times and temperatures are listed in Table III. The applied temperature range was based on Differential Thermal Analysis measurement results from Baldan *et al.*^[31] for conventional cast MAR-M247 material.

Complementary HIP heat-treatments were investigated, as HIP processing is a common requirement for designated safety relevant MAR-M247 applications within turbine engines. The HIP cycle was performed at *Bodycote Haag-Winden, Germany* with industrial scale equipment, followed by a solution heat-treatment and a subsequent two-step aging. The common subsequent MAR-M247 two-step aging is needed to achieve the required γ/γ' and carbide microstructure.

Furthermore, a combined HIP-fast cooling and two-step aging cycle was performed in a HIP furnace at *Quintus Technologies in Västerås, Sweden*. Table III states applied heat-treatment parameters and equipment.

D. Microstructural and Mechanical Investigation

For microstructural evaluation of the as-built and heat-treated specimens, metallographic cross-sections were prepared. To reveal microstructure features, a *V2A* etchant (100 cm^3 HCl, 100 cm^3 H_2O , 10 cm^3 HNO_3 , 0.2 to 2 cm^3 *Dr. Vogels Sparbeize*) heated to 70 $^\circ\text{C}$ was used for sample contrasting. Imaging was performed using a DM6M optical microscope from Leica and a Phenom XL tabletop SEM.

Vickers HV1 hardness measurements were carried out on a Struers Duramin 40 hardness tester. Stain-controlled tensile tests at elevated temperatures (DIN EN ISO 6892-2) were performed on a Zwick Z150TL, with green laser extensometer and round M10 threaded $d_0 = 6 \text{ mm}$ sample geometry. Creep-rupture tests on DS material according to ISO 204:2009 were conducted at *Element Materials Technology Pilsen, Czech Republic*. Tests were performed in the temperature range of 760 $^\circ\text{C}$ to 980 $^\circ\text{C}$ and 100 to 690 MPa stress regime, respectively.

III. RESULTS AND DISCUSSION

A. Microstructure of EBM Alloy 247 in As-Built Condition

The produced specimens are technically dense (specimen bulk material density $> 99.8 \text{ pct}$) and no critical cracks could be detected. A defect density $< 0.15 \text{ 1}/\text{mm}$ and defects with feret diameters $\leq 150 \mu\text{m}$ were rated as tolerable.

An overview of present EBM Alloy 247 grain structures in this work are shown in Figure 5. The grain microstructure could be controlled from equiaxed to columnar grains by adapting melting parameters as they define the melt pool shape, solidification velocity and temperature gradients. The polycrystalline material revealed equiaxed and isotropic grains, while the columnar material was highly anisotropic. The ability to control the degree of grain anisotropy enabled the opportunity for an *in-situ* tailoring the microstructure on demand within a component like a turbine blade.

Tailoring microstructure capability of EBM was already demonstrated in the literature for other Ni-based Superalloys like IN718^[32,33] and

Table I. Nominal Composition of MAR-M247^[30] and Chemical Composition of the Alloy 247 Powder Used for This Study in wt pct (Leco ON736 for O and N, ICP-OES for All Other Elements)

Element	Cr	Co	Mo	W	Ta	Al	Ti	Hf	C	B	Zr	Si	O	N
Nominal	8.4	10	0.6	10	3	5.5	1	1.4	0.15	0.015	0.05			
Powder	8.31	9.75	0.62	10.13	3.00	5.58	1.06	1.20	0.17	0.01	0.05	0.04	70 ppm	49 ppm

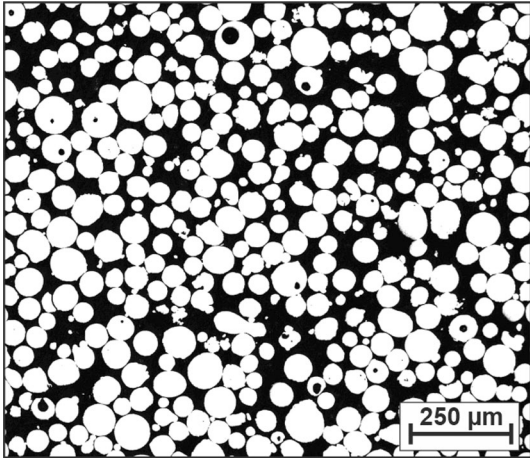


Fig. 3—Powder cross-section micrograph of Alloy 247 powder used for EBM manufacturing. Some irregular-shaped particles, as-well as minor gas pores and satellites could be observed but were in a typical range for gas atomized powder.

Haynes 282,^[34] but at the time of this study not for high-gamma prime alloys with increased crack sensitivity.

For investigation of the grain microstructure evolution during processing, the resulting melt pool shape is of particular importance and was determined for process parameters 1–6 (see Table II) in the last melted layer using etched longitudinal cross-sections. The result was compared to the corresponding bulk microstructure of each specimen in Figure 6. If process parameters leading to a distinct sharp and deep melt pool (parameter 1 and 2) are used, a polycrystalline microstructure was achieved. The mean grain size for poly crystalline material in this study was $\sim 35 \mu\text{m}$ containing grains between 3 to $700 \mu\text{m}$. In contrast to this, if a plain and broad melt pool was generated (parameter 5 and 6), a highly anisotropic and fully columnar microstructure was achieved. Parameters 3 and 4 led to a kind of hybrid microstructure containing fractions of columnar and equiaxed grains.

These observations were in a good agreement with findings in the literature about microstructure evolution in EBM processing of IN718 and CMSX-4.^[32,35,36] Derived from the angle of the solidification direction at the liquid/solid interface of the melt pool, where solidification velocity and temperature gradient are perpendicular to the interface. Thus, a sharp and deep melt pool offers a high angle at the interface, epitaxial growth is suppressed by new grain formation and lead to an equiaxed microstructure. Hence, reduced

solidification angles lead to distinct columnar or hybrid microstructures.

A comprehensive summary on the current understanding about microstructure and mechanical properties of AM processed Ni-based superalloys is given by the recent review from Adomako *et al.*^[37]

The as-built EBM Alloy 247 microstructure is depicted in detail in Figure 7. Optical microscopy of an etched cross-section showing the fully developed and homogenized microstructure consisting of γ/γ' , fine and homogeneous distributed primary carbides within the grains/matrix and secondary carbides at grain boundaries. The cuboidal γ' precipitates within the γ matrix are highlighted in the SEM image (Figure 7 upper right) and the overall γ' -volume content is about ~ 61 pct. The size of the γ' precipitates depends on the height of the produced specimens and EBM processing time. This effect can be explained by the *in-situ* heat-treatment during EBM processing^[20] corresponding to a decrease in hardness from top to bottom of an as-built specimen which can be seen in Figure 10.

In comparison to findings for EBM processing of CMSX-4,^[25] a similar micro dendritic segregation behavior in the as-built condition could not be observed for the investigated Alloy 247 specimens within the applied process parameter range (see Figure 7). As a conclusion, chemical segregation remained on such a small scale and the *in-situ* heat-treatment at EBM process temperature $> 1000 \text{ }^\circ\text{C}$ is sufficient for a homogenization of the material already in the as-built condition.

B. Microstructure of EBM Alloy 247 After Heat-Treatment Procedure

For application of Alloy 247 in a turbine engine a certain γ' size and carbide morphology is required and controlled by a subsequent heat treatment. Thus, heat-treatment is crucial to fulfill structural requirements of a component in terms of creep. For cast MAR-M247 material a standard heat-treatment typically consists of a super-solvus solution heat-treatment (SH) followed by a two-step aging procedure at $1080 \text{ }^\circ\text{C}$ and $900 \text{ }^\circ\text{C}$. The effect of SH temperatures, holding times and different aging conditions for cast material was discussed in the work from Baldan *et al.*^[31] As the current EBM material showed almost no segregation, SH holding times could be reduced to a minimum to obtain γ' in solution for achieving a homogenous distribution as well as a partial solution and re-precipitation of secondary carbides within the specimens. Based on the SH results for EBM processed

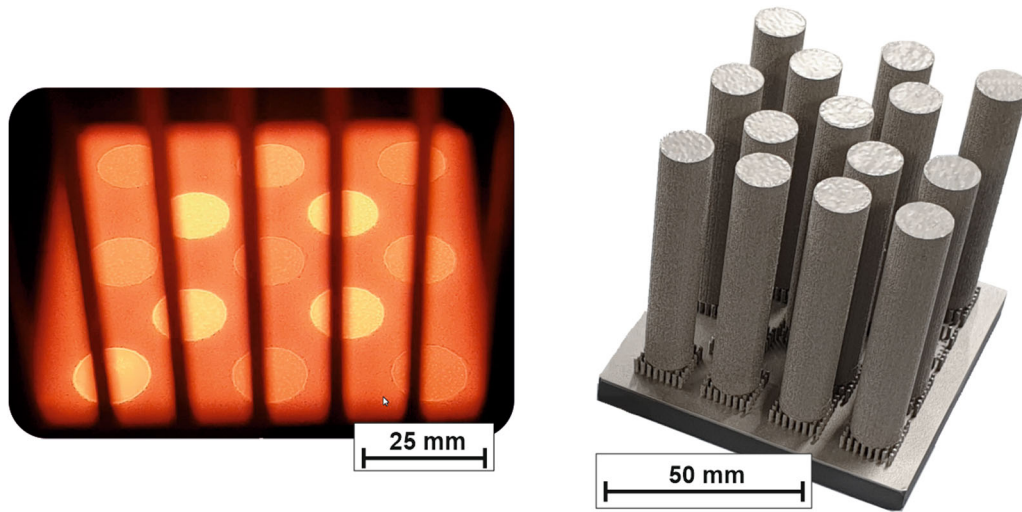


Fig. 4—Glowing EBM powder bed and specimens before recoating of a new powder layer (left). The temperature within the test specimens is > 1000 °C. Typical build showing cylindrical EBM Alloy 247 specimens for mechanical testing on a start plate (right).

Table II. Process Parameters Used for Microstructure Evolution Investigation and Mechanical Testing

Parameter	Volume Energy [J/mm ³]	Beam Power [W]	Line Offset [μm]	Beam Velocity [mm/s]	Focus Offset [mA]	Layer Thickness [μm]
1	120	600	200	500	15	50
2	90	600	200	667	15	50
3	106	596	150	750	15	50
4	94	604	150	857	15	50
5	135	540	100	800	15	50
6	80	480	300	400	35	50
7	137	480	200	250	30	70

The acceleration voltage was kept constant at 60 kV.

Table III. Heat-Treatment Parameter for Solution Heat-Treatment Study and HIP Heat-Treatments and Standard Two-Step Aging Parameter which were Used for This Study

	Temperature (°C)	Holding Time	Pressure	Cooling	Equipment
Solution Heat-Treatment Study	1180 1200 1220 1240 1260 1295	30 min 30 min 30 min 30 min 30 min 60 min		air	Narbertherm LHTC 08/15
HIP Traditional	1240	4 h	1000 bar	furnace	Bodycote
HIP Fast Cooling	1245	4 h	1500 bar	Argon quenching	Quintus
Aging 1	1080	4 h		air/argon in HIP combi cycle	Narbertherm LHTC 08/15 and Quintus
Aging 2	900	8 h			

CMSX-4,^[25] a 30 minutes holding time was chosen to secure a homogenous heat distribution within the specimens in this study (see Table III).

Micrographs of EBM material after only SH and air quenching and after SH and a two-step aging can be seen in Figure 8. As expected from published DTA measurements and ThermoCalc calculations from

Reference 31, for sub solvus (< 1240 °C) SH only a partial solution of smaller γ' precipitates was achieved and coarsening of larger γ' precipitates can be observed. Only for the specimen held at 1180 °C some remaining secondary precipitated $M_{23}C_6$ carbides were seen at grain boundaries. For super-solvus SH above 1240 °C, all γ' and secondary carbides were in solution, only the



Fig. 5—Typical EBM Alloy 247 grain microstructures within specimens of \varnothing 15 mm. The process parameters are defining melt pool shape, solidification velocity and temperature gradients and control whether a poly crystalline and equiaxed (left) or a highly anisotropic columnar (center) grain microstructure is remaining in the specimens. Local tailoring of the microstructure was possible as-well and demonstrated by alternating PS and DS in certain z-heights (right).

primary carbides were remaining well-distributed within the bulk material. Air quenching of super-solvus treated material led to ultra-fine reprecipitation of γ' . No recrystallization or grain growth effects could be observed during all HT investigations. Therefore, the EBM as-built grain microstructure remained after heat-treatment and is the foundation for a localized grain microstructure control in heat-treated components. This is of importance and in contrast to L-PBF processed Alloy 247 where recrystallization effects during HT reduce the anisotropy of AM microstructures and impact material performance.^[38] The main difference between recrystallization and no recrystallization between both technologies can be explained by a lower level of residual stresses in EBM material due to elevated process temperatures causing an *in-situ* stress relief within the components.

By applying the two-step aging, secondary precipitated $M_{23}C_6$ carbides were reprecipitated at the grain boundaries in a chain configuration independent of a prior sub- or super-solvus SH. The partial dissolution of the γ' below 1240 °C (sub-solvus SH) led to coarser γ' particle size after aging than in super-solvus SH treated material, where all γ' was in solution prior to aging. Varying super-solvus SH temperatures between 1240 °C and 1260 °C show no significant impact on the γ' precipitation size. Based on the results of this HT study, a super-solvus HT at 1240 °C is recommended for EBM Alloy 247 material to achieve the desired size and distribution of γ' and carbides.

C. HIP and Heat-Treatment Investigation of EBM Alloy 247

Defects like pores and micro-cracks cannot be completely removed in conventional casted CC and DS Alloy 247 components. Consequently, a subsequent HIP heat-treatment is commonly applied to ensure

component performance in service. This approach was also applied to EBM manufactured Alloy 247 components. Therefore, PX EBM material was post processed with HIP + SH + two-step aging according to Table III to close potential remaining defects in the bulk material prior to testing.

Figure 9 (top row) shows the resulting microstructure after “traditional” subsequent HIP and HT procedure for PX material in both directions. The top left panel shows the perpendicular direction the center and right panel shows the build direction for two magnifications. Similar to the results in the HT study, primary carbides were finely distributed within the bulk material and secondary carbides were well precipitated at the grain boundaries.

Despite the traditional HIP and HT procedure, a combined HIP and HT cycle was applied to EBM Alloy 247 DS material in a HIP furnace with fast cooling capabilities. The benefit of this process route is the elimination of SH equipment and process time. The resulting microstructure is depicted in Figure 9 (bottom row) in both directions, perpendicular (bottom left) and in build direction for two magnifications (bottom center, bottom right). In contrast to PX EBM material, primary carbides were more pronounced in lines following the columnar grain morphology. Secondary carbides were mostly distributed in a chain configuration at the grain boundaries and did not form carbide networks or carbide films along the grain boundaries.

Both HIP heat-treatments led to good microstructural properties. No defects as well as no recrystallization or grain growth were observed in the bulk material. Possible remaining segregations were not observed and a fully homogenized material exhibiting a homogeneous γ' size and distribution was obtained. This highlights the potential in terms of cost saving by exploiting a combined HIP and heat-treatment cycle for Alloy 247 EBM components with consistent material quality.

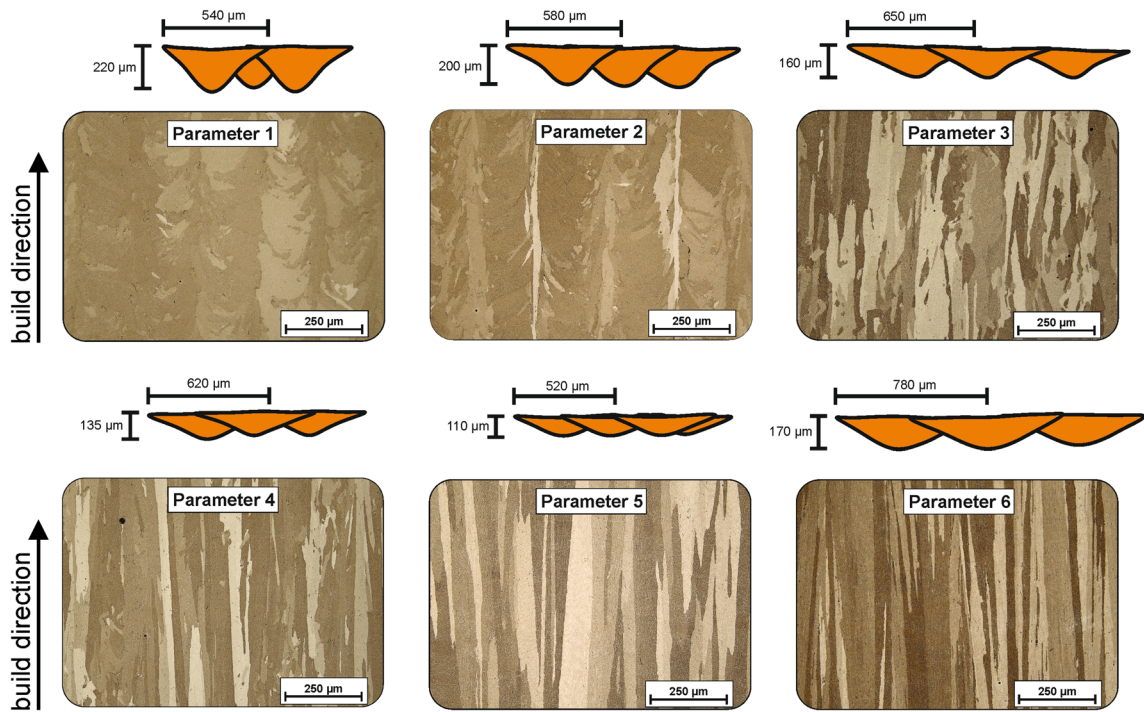


Fig. 6—Melt pool shape, size and corresponding bulk grain microstructure using process parameters from Table II. The melt pool shape can be correlated to the formed grain microstructure. Distinct and sharp melt pools shapes lead to more equiaxed and plain form to anisotropic grain microstructures.

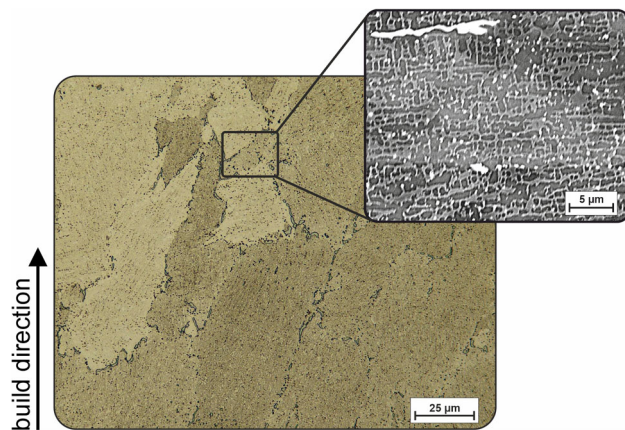


Fig. 7—Typical EBM Alloy 247 as-built microstructure (PX), OM and SEM BSE contrast imaging.

D. Mechanical Room and High-Temperature Properties of EBM Alloy 247

To evaluate the potential of EBM Alloy 247, mechanical properties were investigated for poly crystalline (PX) and directionally solidified (DS) EBM test specimens and compared with other manufacturing technologies.

Vickers hardness measurements performed along the build direction in as-built and heat-treated specimens are shown in Figure 10. The as-built state shows a hardness of ~ 510 HV1 at the sample top surface and ~ 440 HV1 for material consolidated > 5 mm below the top surface. The increased hardness at the

top surface region can be explained by the occurrence of very fine γ' precipitates within this region. The top surface material was melted last and has seen the shortest exposure time during *in-situ* EBM heat-treatment resulting in a γ' precipitation growth over time. Thus, hardness values could be directly correlated to a certain γ' size exhibiting a gradient along the build direction which is typical for EBM fabricated high γ' Superalloys and were in a good agreement to reported results for EBM SX CMSX-4 material.^[39] An increased hardness level for EBM Alloy 247 could be caused by the PX microstructure and the presence of carbides in this alloy.

After applying a full heat-treatment procedure, a hardness of about ~ 380 to 390 HV1 was measured across the full sample height indicating a mean γ' size of about 0.4 to 0.5 μm homogeneously distributed within the specimen.^[11] While as-built EBM hardness values were in good accordance to micro-hardness tests conducted on heat-treated L-PBF and Binder Jet CM 247LC material (~ 450 HV0.1), the heat-treated EBM Alloy 247 showed a decrease in hardness of ~ 60 to 70 HV.^[16,40] Lower values in HT EBM condition compared to stated reference data may be caused by differences in γ' size and quantity of carbides within Alloy 247. Differences could also partially be caused by deviating measurement methods between HV0.1 and HV1.

Tensile test results at room- and elevated temperature for EBM Alloy 247 with poly crystalline (PX EBM - HIP HT) and directionally solidified (DS EBM - HIP HT) microstructure are shown in Figure 11. The results were

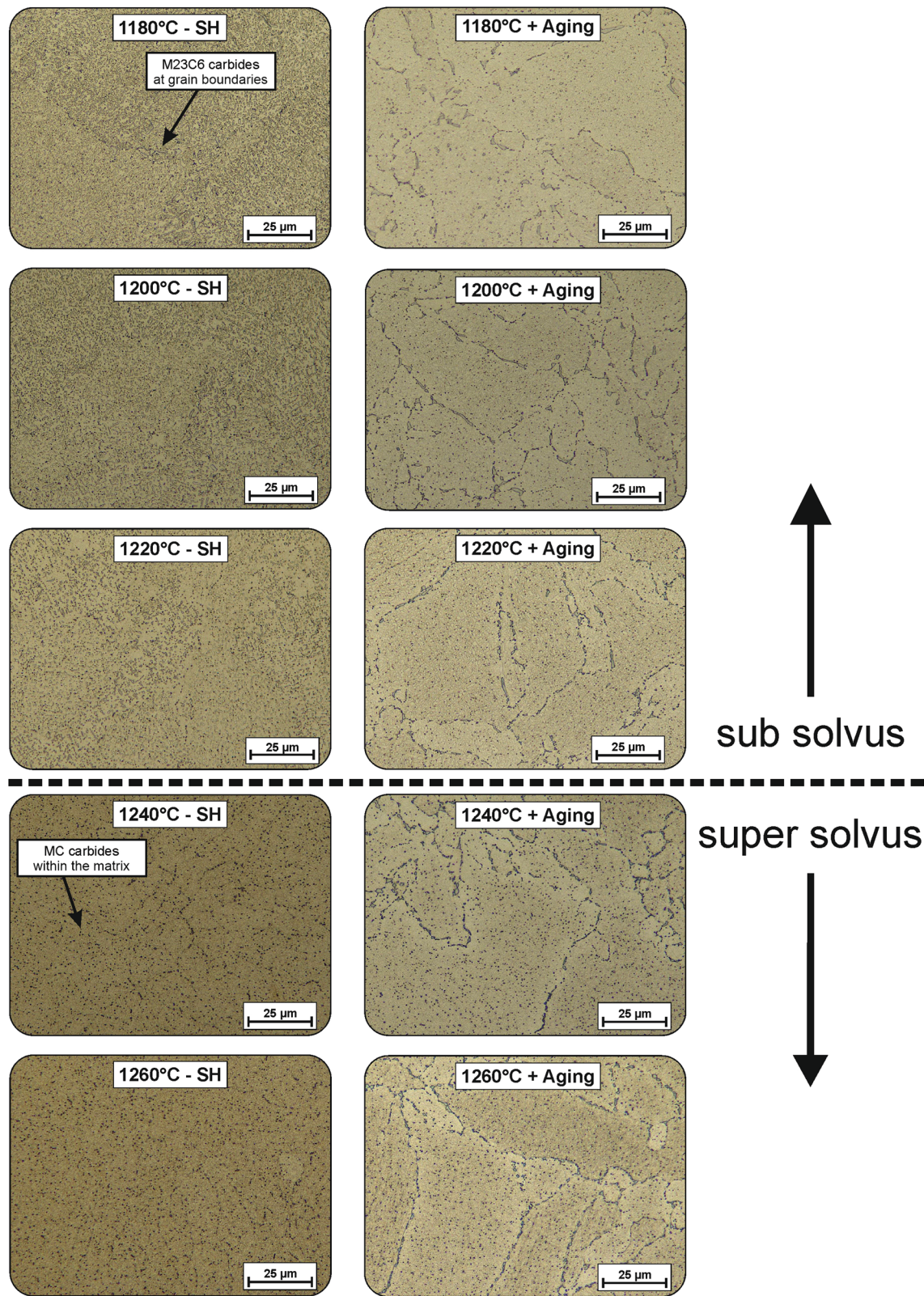


Fig. 8—Micrographs of EBM Alloy 247 after different solution heat-treatment (SH) temperatures and corresponding microstructure after applying a two-step aging. Below 1200 °C secondary precipitated $M_{23}C_6$ carbides are remaining at grain boundaries. Up to 1240 °C coarse γ' is not completely dissolved. Above 1240 °C carbides and γ' phase is resolved, only fine primary MC carbides remain homogeneously distributed within the gamma-matrix. Aging leads to re-precipitation of $M_{23}C_6$ carbides in a chain-like shape at grain boundaries.

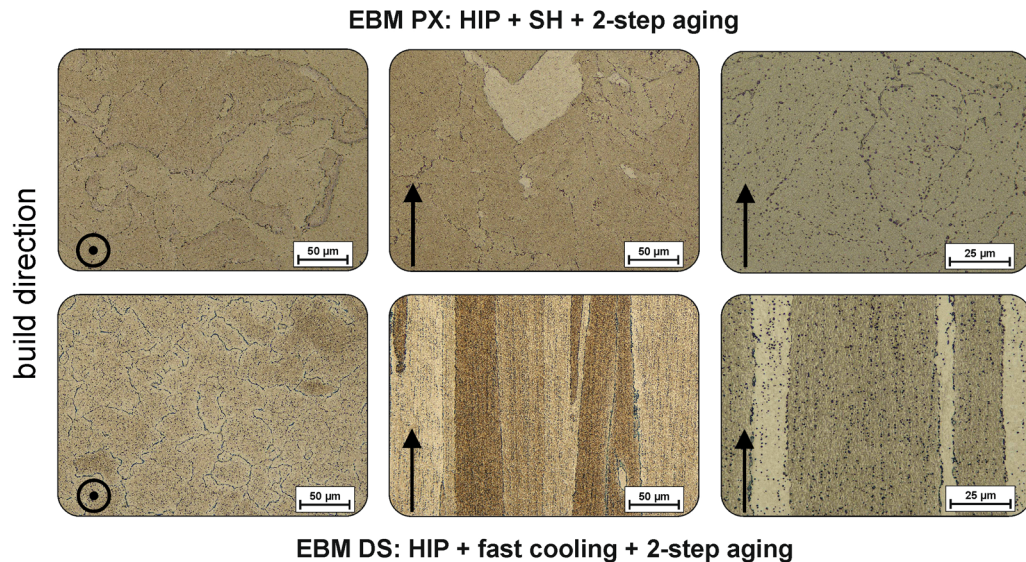


Fig. 9—Micrographs of a traditional HIP + SH + 2-step aging heat-treated PX EBM specimen (top row). Micrographs of a combined HIP + 2-step aging heat-treatment of a DS EBM specimen using fast cooling HIP capabilities (bottom row). Grain microstructure has an impact on distribution of the primary carbides. In DS configuration the carbides follow the columnar morphology.

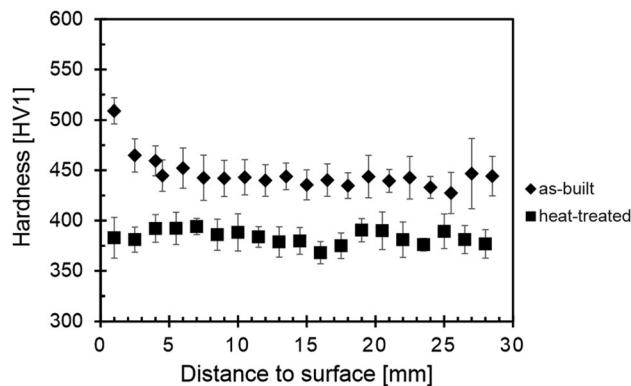


Fig. 10—Hardness of poly crystalline EBM Alloy 247 in as-built and heat-treated condition. The hardness decreases the initial 5 mm from the top surface in as-built material. This can be explained by a time dependent growth of γ' precipitates due to *in-situ* heat-treatment at EBM processing. A homogenous hardness level across the entire sample was achieved in heat-treated condition.

compared to values from the literature values for casted CM247 LC^[41] with varying grain sizes (Casting PX 80 to 90 μm , PX 150 to 200 μm , PX 2–3 mm) and Binder Jet material data for R108 (Binder Jet PX).^[42] R108 is a CM247 LC derivate developed by General Electric and shows similar mechanical properties.

The yield tensile strength (YTS) of tested PX EBM material showed consistent results with the PX cast reference from CM247 LC. At room temperature, PX EBM and the cast PX reference material showed a yield strength between 950 and 1000 MPa, which is in agreement with other casted MAR-M247 results reported in Reference 43 and PX Binder Jet material.^[40] DS EBM material showed a slightly lower YTS at room temperature corresponding to the elastic modulus dependency of crystallographic orientation in DS

material. Due to the yield strength anomaly of γ' hardened Ni-based superalloys, the typical increase of yield strength up to temperatures around 760 °C was observed with a maximum yield strength between 950 and 1050 MPa. For temperatures above 760 °C a continuous decrease in yield strength could be observed as expected. DS EBM material shows the highest YTS strength here. The results are even comparable to conventional cast PX MAR-M247 material data used in industrial application, recently published by Tang *et al.*^[44]

For ultimate tensile strength (UTS) at room temperature, PX EBM and Binder Jet material offered the highest strengths of around 1400 MPa most likely due to the fine grain sizes. At 550 °C PX EBM material exhibited superior UTS compared to EBM DS, cast Reference PX and Binder Jet processed material. For higher test temperatures, DS EBM also shows the highest UTS due to grain anisotropy and Binder Jet material showed to lowest UTS caused by the very fine PX grain microstructure.

At room temperature, PX EBM and DS EBM material showed ~9 pct fracture elongation and is in accordance with fine-grained cast reference material. Tang *et al.* have reported an even lower elongation for cast PX MAR-M247 material < 5 pct.^[44] An interesting observation is the EBM material fracture elongation of 10 to 15 pct at ≥ 760 °C for both, PX and DS configuration. In comparison to PX cast reference and Binder Jet material, the EBM material showed increased fracture elongation at this temperature region, which coincide with cast DS material data reported in Reference 43. While the DS fracture elongation is aligned with literature data,^[2] one potential explanation for the increased PX.

EBM fracture elongation could be a distinct texture/degree of anisotropy in the microstructure of PX EBM material. This should be investigated further in the

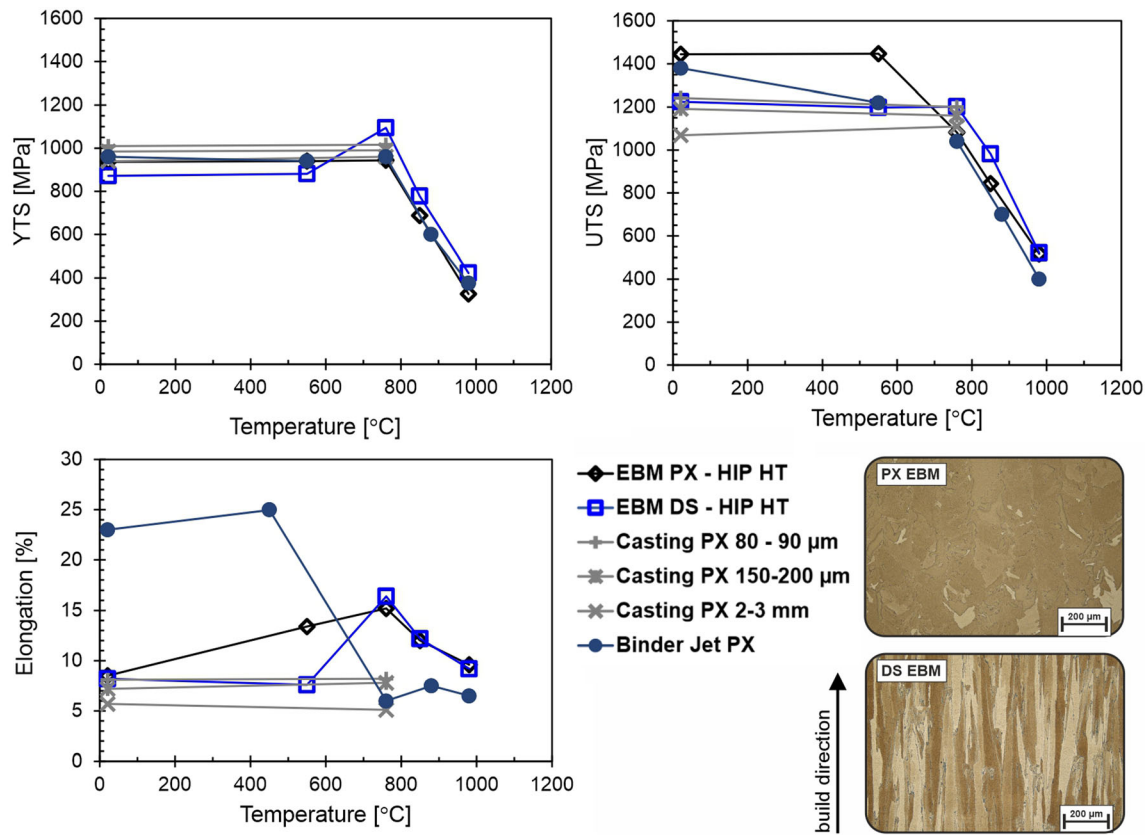


Fig. 11—Tensile properties of HIP and heat-treated EBM Alloy 247 in PX and DS configuration compared to data from conventional casted and heat-treated CM 247LC with three different grain sizes (Casting PX)^[41] and data from Binder Jet processed R108.^[42]

future and proven by utilizing SEM microscopy and EBSD measurements. Binder Jet material showed the highest room temperature elongation of about 23 pct and stable elongation up to 500 °C, followed by a substantial drop at 760 °C to ~ 6 pct. The drop is likely caused by the ultrafine grain size of Binder Jet material. This is in contrast to the results of Binder Jet produced MAR-M247 by Dahmen *et al.*, where a maximum of 4 pct elongation at room temperature was reported and referred to embrittlement due to grain boundary carbide formation.^[40]

Reflecting these tensile test results led to the conclusion that material homogeneity as well as carbide size, morphology and distribution have a strong effect especially in terms of elongation. This should be investigated more in detail in further investigations using advanced characterization methods.

Determination of creep properties for EBM Alloy 247 were performed and compared to literature data for conventional cast material in PX and DS condition as well as to other AM processing technologies.^[12,13,16] The Larson–Miller plot in Figure 12 show the determined DS EBM Alloy 247 creep results (tested in DS orientation) values from literature for a comparison. Baselines are the dotted lines for conventional cast PX and DS material from Reference 45. EBM DS material creep

results for selective temperatures and load conditions show that creep properties better than PX and comparable to DS casting could be achieved. Indications for superior performance in the high-stress low-temperature regime could be recognized. The test at 950 °C and 100 MPa conditions was stopped at about 2330 hours and 0.51 pct elongation after exceeding PX cast properties for capability demonstration.

The creep properties for fine-grained CM 247LC presented in Reference 41 were equal to the PX MAR-M247 baseline, so both alloys are expected to show similar creep life for polycrystalline condition. However, reported L-PBF CM 247LC creep life in Reference 16 was significantly lower. An explanation for this inferior creep performance can be found in the reported fine-grained microstructures of about 30 μm. It is well-known that such as fine-grained material is leading to poorer creep properties especially within the high-temperature regime. If this is considered and compared for the polycrystalline EBM Alloy 247 grain sizes from this study, it is obvious that similar creep properties can be expected here. This can be seen in the Larson–Miller plot (Figure 12) for a stress level of 200 MPa, where the grain size and grain morphology affect the creep performance within a broad range of $P = 46$ to 50.

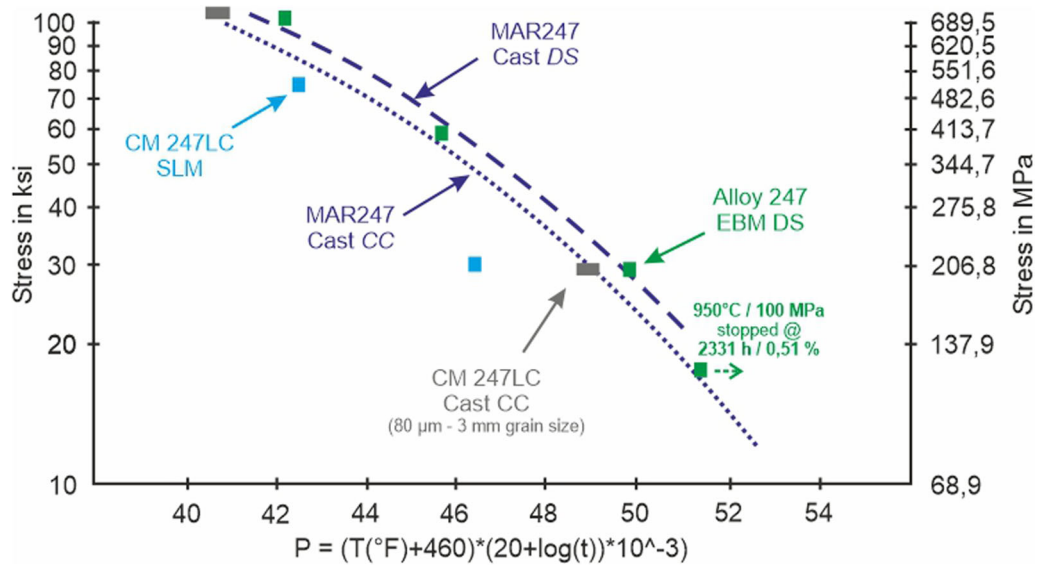


Fig. 12—Larson-Miller plot to rupture life of DS EBM Alloy 247 material compared to data from PX and DS cast MAR-M247,^[45] data from L-PBF manufactured CM 247LC^[16] and data from fine-grained conventionally casted CM 247LC.^[41]

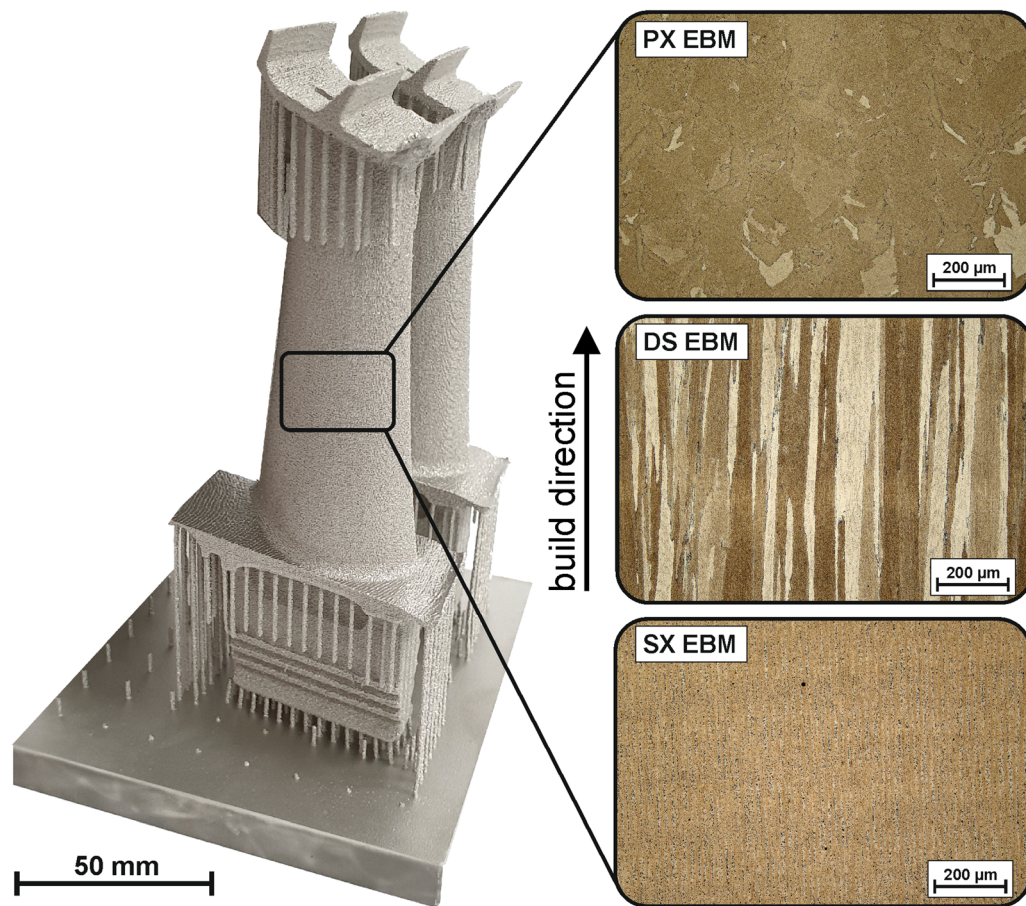


Fig. 13—Generic Alloy 247 turbine-blade demonstrator manufactured by EBM with support structures on a start-plate. The three microstructure images show exemplary the potential for unique tailored or gradient microstructures on demand in turbine blades using EBM. Besides PX and DS microstructures, a single-crystalline microstructure in bulk material can be achieved and will may expand the AM manufacturing capabilities of Alloy 247 even more in the future.

Grain size-controlled creep properties for conventional processed material are well understood. However, the results from this study led to the question why a “micro-DS” EBM grain structure achieve similar creep properties as a “coarse-DS” grain structure in investment casting? This finding strengthens the theory of Arzt and Singer^[46] from the 80’s where they could show that not only grain size defines creep-rupture properties. Rather the grain aspect ratio has a more significant impact on creep-rupture life. Their theory is based on a change in crack-propagation mechanism from intergranular to transgranular mode if the grain aspect ratio is increasing. The transition point in their investigations was determined to a ratio of about 20. Above this ratio creep-rupture life stays mainly constant independent from the aspect ratio. In the present study, a ratio of about 40 to 100 was determined by measuring random chosen grains in DS EBM specimens. This could explain the excellent creep-rupture properties of micro-DS EBM Alloy 247 material and could even endorse the theory from Kurz and Singer for a grain aspect ratio ≥ 20 .

Introducing high anisotropy grain microstructures results in orientation dependent creep-rupture properties. Having this in mind and based on work which has been done in literature for conventionally processed material, transversal creep properties of DS microstructures are expected to be comparable to polycrystalline material.^[45,47] Thus, a reduction of transversal creep-rupture properties must be expected for EBM manufactured material and should be investigated more in detail in future research work.

IV. CONCLUSIONS

The crack-prone Ni-based Superalloy Alloy 247 could successfully be fabricated by EBM AM in this work and the following conclusions could be made:

- By adopting local process parameter during EBM processing an *in-situ* grain morphology and microstructure control was possible. This was achieved by adapting melt pool shape, solidification velocity and temperature gradients. Polycrystalline or columnar microstructures could be achieved as well as tailored gradient microstructures.
- Tensile properties were comparable to or better than conventionally processed material. DS EBM material provided superior strength- and elongation values in comparison to other AM manufacturing technologies at temperatures above 700 °C.
- Directionally solidified (DS) EBM material achieved similar creep performance as DS cast material, despite the observed “micro-DS” grain structure in EBM. Existing reference data for L-PBF and Binder Jet fabricated material was inferior to EBM DS condition. Creep properties were strongly depending on grain morphology which reveals the possibility to optimise creep performance by EBM microstructure control.
- As-built EBM Alloy 247 material showed no noticeable dendritic segregation behavior and exhibited a fully developed microstructure containing > 60 vol

pct γ' phase. Carbides were finely distributed within the grains and at grain boundaries. Due to high EBM process temperatures (> 1000 °C) a gradient in γ' size is present in as-built condition.

- The solution heat-treatment holding time could be reduced due to the homogeneity of the EBM material in the as-built condition. The holding time is solely required to secure a homogeneous temperature within the component. A suitable super-solvus heat-treatment was identified at 1240 °C for 30 minutes. No recrystallization effects or cracking issues were observed during heat-treatment of EBM fabricated material.
- HIP heat-treatment could secure defect-free material and can be used as a combined HIP + HT processing step, saving time and cost. Sequential and combined HIP + HT led to similar microstructures, defined by homogenized material exhibiting plain γ' size and distribution. Finely distributed carbides within the grains and re-precipitated carbides at grain boundaries arranged in a chain configuration were achieved.

The presented results highlight the EBM capability to process high gamma prime superalloys such as Alloy 247. Local microstructure control of components, combined with excellent directionally solidified creep properties are seen as foundations for further development and adaption focused on development and adoption of the EBM technology for turbine engine component production. One exemplary application that will utilize these benefits are turbine blades as shown in Figure 13. Besides the presented poly crystalline and columnar/directionally solidified microstructure capabilities, EBM also has the potential for single-crystalline manufacturing of Ni-based Superalloys in the long term. This was exemplary demonstrated for Alloy 247 by applying process conditions published in Reference 39 (see Figure 13). Further highlighting the potential of EBM processing for future engine applications.

CONFLICT OF INTEREST

This work was funded through GE Additive Gothenburg, Sweden. The manuscript is approved by all authors for publication.

OPEN ACCESS

This article is licensed under a Creative Commons Attribution 4.0 International License, which permits use, sharing, adaptation, distribution and reproduction in any medium or format, as long as you give appropriate credit to the original author(s) and the source, provide a link to the Creative Commons licence, and indicate if changes were made. The images or other third party material in this article are included in the article’s Creative Commons licence, unless indicated otherwise in a credit line to the material. If material is

not included in the article's Creative Commons licence and your intended use is not permitted by statutory regulation or exceeds the permitted use, you will need to obtain permission directly from the copyright holder. To view a copy of this licence, visit <http://creativecommons.org/licenses/by/4.0/>.

REFERENCES

1. K. Harris, and R.E. Schwer: Vacuum induction refining mm 0011 (MAR M-247) for high integrity turbine rotation parts, (*Cannon-Muskegeon Coroperation*, Michigan), <https://cannonmuskegon.com/technical-info/white-papers/>. Accessed 30 October 2022.
2. K. Harris, G. Erickson, R. Schwer: *Fifth International Symp. on Superalloys*, 1984.
3. S. Griffiths, H. Ghasemi Tabasi, T. Ivas, X. Maeder, A. De luca, K. Zweiacker, R. Wrobel, J. Jhabvala, R.R. Loge, and C. Leinenbach: *Addit. Manuf.*, 2010, vol. 36, p. 101443.
4. D. Dye, O. Hunziker, and R. Reed: *Acta Mater.*, 2001, vol. 49, pp. 683–97.
5. J. DuPont and T. Anderson: *Hot Cracking Phenomena Welds*, 2011, vol. III, pp. 429–39.
6. M. Zhong, H. Sun, W. Liu, et al.: *Scripta Mater.*, 2005, vol. 53, pp. 159–64.
7. R. Sidu, O. Ojo, and M. Chaturvedi: *Metall. Mater. Trans. A*, 2009, vol. 61A, pp. 150–62.
8. A. Egbewande, R. Buckson, and O. Ojo: *Mater. Charact.*, 2010, vol. 61, pp. 569–74.
9. K.M. Cam: *Int. Mater. Rev.*, 1998, vol. 43, pp. 1–44.
10. M.B. Henderson, D. Arrell, M. Hoebel, et al.: *Sci. Technol. Weld. Joining*, 2004, vol. 9, pp. 13–21.
11. M. Ramsperger: *PhD dissertation*, Erlangen, 2018.
12. H. Hilal, R. Lancaster, S. Jeffs, J. Boswell, D. Stapleton, and G. Baxter: *Materials*, 2019, vol. 12, p. 1390.
13. O. Adegoke, J. Andersson, H. Brodin, and R. Pedersen: *Metals*, 2020, vol. 10, p. 996.
14. S. Catchpole-Smith, N. Aboulkhair, L. Parry, C. Tuck, I. Ashcroft, and A. Clare: *Addit. Manuf.*, 2017, vol. 15, pp. 113–22.
15. J. Boswell, D. Clark, W. Li, and M. Attallah: *Mater. Design*, 2019, vol. 174, p. 107793.
16. Y. Tang, C. Panwisaws, J. Ghousoub, Y. Gong, J. Clark, A. Nemeth, D. McCartney, and R. Reed: *Acta Mater.*, 2021, vol. 202, pp. 417–36.
17. R. Engeli, T. Etter, S. Hövel, et al.: *J. Mater. Process. Technol.*, 2016, vol. 229, pp. 484–91.
18. L. Murr, E. Martinez, X. Pan, et al.: *Acta Mater.*, 2013, vol. 61, pp. 4289–96.
19. B. Lim, H. Chen, Z. Chen, N. Haghdadi, X. Liao, S. Primig, S. Babu, A. Breen, and S. Ringer: *Addit. Manuf.*, 2021, vol. 46, p. 102121.
20. M. Ramsperger, R. Singer, and C. Körner: *Metall. Mater. Trans. A*, 2016, vol. 47A, pp. 1469–80.
21. M. Ramsperger and C. Körner, *Superalloys 2016: Proceedings of the 13th International Symposium on Superalloys*, 2016 Seven Springs.
22. E. Chauvet, C. Tassin, J. Blandin, R. Dendievel, and G. Martin: *Scripta Mater.*, 2018, vol. 152, pp. 15–19.
23. E. White, T. Prost, R. Napolitano and I. Anderson, *Ames*, 2019, IA (United States).
24. Y. Lee, M. Kirka, A. Sridharan, A. Okello, R. Dehoff, and S. Babu: *Metall. Mater. Trans. A*, 2018, vol. 49A, pp. 5065–79.
25. M. Ramsperger, L. Mujica Roncery, I. Lopez-Galilea, R. Singer, W. Theisen, and F. Körner: *Adv. Eng. Mater.*, 2015, vol. 17, pp. 1486–93.
26. D. Bürger, A. Parsa, M. Ramsperger, C. Körner, and G. Eggeler: *Mater. Sci. Eng. A*, 2019, vol. 762, p. 138098.
27. C. Körner, M. Ramsperger, C. Meid, D. Burger, P. Wollgram, M. Bartsch, and G. Eggeler: *Metall. Mater. Trans. A*, 2018, vol. 49A, pp. 3781–92.
28. B. Rutttert, M. Ramsperger, L. Mujica Roncery, I. Lopez-Galilea, C. Körner, and W. Theisen: *Mater. Design*, 2016, vol. 110, pp. 720–27.
29. C. Meid, A. Dennstedt, M. Ramsperger, J. Pistor, B. Rutttert, I. Lopez Galilea, W. Theisen, C. Körner, and M. Bartsch: *Scripta Mater.*, 2019, vol. 168, pp. 124–28.
30. R. Bürgel, H. Maier and T. Niendorf, *Handbuch Hochtemperatur-Werkstofftechnik*, Vieweg+ Teubner Wiesbaden, 2006.
31. R. Baldan, R. da Rocha, R. Romasiello, et al.: *J. Mater. Eng. Perform.*, 2013, vol. 22, pp. 2574–79.
32. H. Helmer, A. Bauereiss, R. Singer, et al.: *Mater. Sci. Eng. A*, 2016, vol. 668, pp. 180–87.
33. M. Kirka, K. Unocic, N. Raghavan, et al.: *JOM*, 2016, vol. 68, pp. 1012–20.
34. P. Fernandez-Zelaia, M. Kirka, S. Dreypondt, and M. Gussev: *Mater. Design*, 2020, vol. 195, p. 109010.
35. J. Pistor, C. Breuning, and C. Körner: *Materials*, 2021, vol. 14, p. 3785.
36. M. Gotterbarm, A. Rausch, and C. Körner: *Materials*, 2020, vol. 10, p. 313.
37. N.K. Adomako, N. Haghdadi, and S. Primig: *Mater. Design*, 2022, vol. 223, p. 111245.
38. O. Adegoke, J. Andersson, O. Ojo, H. Brodin and R. Pederson, *Materials Science and Technology 2019 (MS&T19)*, 2019, Oregon, Portland USA.
39. M. Ramsperger and C. Körner, *Superalloys 2016: Proceedings of the 13th International Symposium on Superalloys*, 2016 Seven Springs, Pennsylvania USA.
40. T. Dahmen, N. Henriksen, K. Dahl, A. Lapina, D. Pedersen, J. Hattel, T. Christiansen, and M. Somers: *Addit. Manuf.*, 2021, vol. 39, p. 101912.
41. H. Huang and C. Koo: *Mater. Trans.*, 2004, vol. 45(2), pp. 562–68.
42. E. Martin, A. Natarajan, S. Kottilingham, and R. Batmaz: *Addit. Manuf.*, 2021, vol. 39, p. 101894.
43. H. Bor, C. Wei, A. Yeh, W. He, H. Wang, and C. Kuo: *Mater. Sci. Forum*, 2014, vol. 783–786, pp. 1153–58.
44. Y.T. Tang, C. Schwalbe, M. Futoma, B. Roebuck, S. Utada, and R.C. Reed: *Metall. Mater. Trans. A*, 2022, <https://doi.org/10.1007/s11661-022-06869-x>.
45. G. Erickson, K. Harris and R. Schwer, *Proceedings of the ASME 1985 International Gas Turbine Conference and Exhibit*, 1985, Volume 4: *Manufacturing Materials and Metallurgy; Ceramics; Structures and Dynamics; Controls, Diagnostics and Instrumentation*, Houston, Texas, USA.
46. E. Arzt and R. Singer, *Superalloys 1984*, 1984, Warrendale, PA, USA.
47. D. Woodford and J. Frawley: *Metall. Trans.*, 1974, vol. 5, pp. 2005–13.

Publisher's Note Springer Nature remains neutral with regard to jurisdictional claims in published maps and institutional affiliations.